

***Particle-mediated nucleation pathways are imprinted in the internal structure  
of calcium sulfate single crystals***

Tomasz M. Stawski<sup>1</sup>, Helen M. Freeman<sup>1,2</sup>, Alexander E.S. Van Driessche<sup>3</sup>, Jörn Hövelmann<sup>1</sup>,

Rogier Besselink<sup>1,3</sup>, Richard Wirth<sup>1</sup>, and Liane G. Benning<sup>1,4,5</sup>

<sup>1</sup>German Research Centre for Geosciences, GFZ, Interface Geochemistry, Telegrafenberg, 14473, Potsdam, Germany;

<sup>2</sup>School of Chemical and Process Engineering, University of Leeds, Woodhouse Lane, LS2 9 JT, Leeds, UK;

<sup>3</sup>Université Grenoble Alpes, CNRS, ISTERre, 1381 Rue de la Piscine, 38610 Gières, Grenoble, France;

<sup>4</sup>Geochemistry Group, Department of Earth Sciences, Free University of Berlin, Malteserstr. 74-100 / Building A, 12249 , Berlin, Germany.

<sup>5</sup>School of Earth and Environment, University of Leeds, Woodhouse Lane, LS2 9 JT, Leeds, UK;

**Keywords:** calcium sulfate; gypsum; bassanite; anhydrite; mesocrystal; non-classical; crystallisation

## Abstract

Calcium sulfate minerals are found under the form of three crystalline phases: gypsum ( $\text{CaSO}_4 \cdot 2\text{H}_2\text{O}$ ), bassanite ( $\text{CaSO}_4 \cdot 0.5\text{H}_2\text{O}$ ), and anhydrite ( $\text{CaSO}_4$ ). Due to its relevance in natural and industrial processes, the formation pathways of these calcium sulphate phases from aqueous solution have been the subject of intensive research. There is a growing body of literature, that calcium sulfate forms essentially through a non-classical nanoparticle- or cluster-mediated crystallisation process. At the early stages of precipitation calcium sulfate crystals grow through the reorganization and coalescence of aggregates rather than through classical unit addition. Here, we show by using low-dose dark field (DF) transmission electron microscopy (TEM) and electron diffraction, that these re-structuring processes by no means continue until a near-perfectly homogeneous single crystal is obtained. Instead the growth process yields a final imperfect mesocrystal of the overall morphology resembling that of a single crystal, yet composed of smaller nano-domains. Hence, our data indicate that organic-free mesocrystal grown by a particle mediated-pathway may preserve a “memory” or “imprint” of the non-classical growth process in the final crystal structure, something that has been largely overlooked until now. Furthermore, the nano-scale misalignment of the structural sub-units within crystals might propagate through the length-scales, and potentially is expressed macroscopically as misaligned zones/domains in large single crystals, e.g. as those observed in some of the giant crystals from the Naica Mine, Chihuahua, Mexico.

## Introduction

Calcium sulfate minerals are abundant in natural and engineered environments under the form of three crystalline phases: gypsum ( $\text{CaSO}_4 \cdot 2\text{H}_2\text{O}$ ), bassanite ( $\text{CaSO}_4 \cdot 0.5\text{H}_2\text{O}$ ), and anhydrite ( $\text{CaSO}_4$ ). Due to its relevance in natural and industrial processes, the formation pathways of these calcium sulphate phases from aqueous solution has been the subject of intensive research in the last few years<sup>1</sup>. Based on small-angle X-ray scattering (SAXS) data, we recently reported that gypsum crystals form through aggregation of sub-3 nm precursor species to several-micron-large morphologies<sup>2</sup>. These aggregates transform into gypsum crystals through the growth, coalescence and re-arrangement of the primary species. Hence, the nucleation of gypsum is essentially a nanoparticle- or cluster-mediated process. Importantly, faceted single crystals produced SAXS patterns, which at low- $q$  were characteristic for internally homogeneous large structures, yet at high- $q$  these patterns contained scattering features originating from nanosized sub-units. These scattering patterns were fitted using a “brick-in-a-wall” surface fractal model, for which we developed a rigorous mathematical description<sup>3</sup>. This “brick-in-a-wall” model implies that sub-units constituting the bricks are clearly distinguishable from each other, leading to a single crystal composed of slightly misaligned crystallographic domains and hence expected to exhibit high mosaicity<sup>4</sup>. In this regard, for nanoparticulate sub-units this “brick-in-a-wall” scattering model is in fact akin to the concept of mesocrystallinity<sup>5-11</sup>.

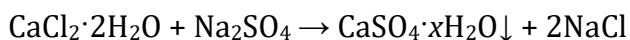
Mesocrystals are single crystals in terms of their crystallographic properties and external forms but they are internally composed of numerous crystalline nanoparticles or sub-domains of similar sizes and shapes. These are arranged in a highly ordered, but spatially separated manner, yet the mesocrystals yield diffraction patterns typical for single crystals. Most commonly mesocrystals are considered as composite assemblies of inorganic particles bound by organic

species<sup>11</sup> (surfactants, macromolecules, small organic molecules etc.), but mesostructured crystals can also form without the involvement of organic species. For example, through a process where stable pre-synthesised nanoparticles are “driven” to arrange themselves to form larger crystals through physical fields such as magnetic, electric or hydration forces, or to minimize their surface area, and thus to lower their free energy<sup>12-16</sup>. Hence, growth proceeds through a non-classical particle-mediated bottom-up process, which can involve aggregation/re-orientation, and/or oriented attachment<sup>6,17,18</sup> of the primary particles. Importantly, such organic-free mesocrystals can form as metastable intermediate phases that are necessary precursors to more internally continuous and stable single crystals, e.g. ferrihydrite transformation to goethite<sup>17,19</sup>, or the formation of rutile from titania nanorods<sup>20</sup>.

At present it is not clear what impact the particle-mediated crystallization pathway<sup>7</sup> has on the internal, and external, structure of the final crystalline phase. We hypothesize that organic-free mesocrystal grown by a particle mediated-pathway may preserve a “memory” or “imprint” of this growth process in the final crystal structure, something that has been largely overlooked until now. To test this hypothesis we built upon our previous work where we have shown that calcium sulphate formation follows such a particle-mediated route, and in the current study we have characterized in detail the internal structure of the different calcium sulphate phases: synthetic gypsum and bassanite, as well as natural anhydrite (from the Naica Mine, Chihuahua, Mexico). We show compelling evidence for the mesostructured character of all these single crystals and consider the origin of their mesocrystallinity in the context of the growth mechanisms of calcium sulfate phases.

## Experimental

CaSO<sub>4</sub> in the form of gypsum (dihydrate, 2H<sub>2</sub>O,  $x = 2$ ) and bassanite (hemihydrate, 0.5H<sub>2</sub>O,  $x = 0.5$ ) was synthesized by reacting equimolar aqueous solutions of CaCl<sub>2</sub>·2H<sub>2</sub>O (pure, Sigma) and Na<sub>2</sub>SO<sub>4</sub> (> 99%, Sigma), based on the following reaction:



Gypsum formed from a mixed solution of a final concentration of [CaSO<sub>4</sub>] of 50 mmol/L at T = 21 °C, and was left under stirring for 2 days. The formed crystals were directly deposited from the mother solution onto a Cu holey carbon TEM grid, dried in air and used for further analyses. Bassanite was synthesised from a mixed solution of a final concentration of [CaSO<sub>4</sub>] of 50 mmol/L and increased salinity of 4.3 mol/L at T = 80 °C for 8 hours. Such high salinity/high-T conditions promoted the reduced activity of water, which resulted in the direct precipitation of metastable hemihydrate<sup>21</sup>. In the next step a solution containing the precipitated crystals was centrifuged at 3000 rpm and the supernatant was decanted. The remaining crystals were dried in air and then deposited onto a TEM grid without and dispersing medium.

Large natural single crystals of gypsum and anhydrite ( $x = 0$ ) were obtained from the Niaca Mine in Chihuahua, Mexico<sup>22</sup>. The used specimen of gypsum was ~3 cm in length and anhydrite was ~1 cm in length, but in fact they were both fragments chipped from larger single crystals (> 1 m in length for gypsum and >5 cm for anhydrite). To analyse such large crystals we prepared ~15 µm x 4 µm sections that were thinned to foils of ~100 nm thick from each of the single crystals using a focused ion beam technique (FEI FIB200) following the standard procedure described in reference<sup>23</sup>. For the purpose of comparison we also prepared in a similar fashion thin foils of fosterite (formally Mg<sub>2</sub>SiO<sub>4</sub>, Mg-rich olivine end member) and olivine ((Mg,Fe<sup>2+</sup>)<sub>2</sub>SiO<sub>4</sub>) single crystals (Fig. S1). Olivines are igneous minerals known to form naturally big and very high

quality single crystals, and as such constitute a good example of materials exhibiting very low mosaicity.

For transmission electron microscopy (TEM) imaging and selected-area electron diffraction (SAED or ED), a Tecnai F20 XTWIN TEM was used at 200 kV, equipped with a field emission gun electron source. Bright-field (BF) and dark-field (DF) images were acquired as energy-filtered images; for that purpose a 20 eV window was applied to the zero-loss peak. For DF-TEM, the selected diffraction spots were selected by the objective aperture depending on the sample (the used diffraction spots are marked in Figs. 1-3 & S1 accordingly). ED patterns were collected using an aperture with an effective diameter of ca. 1  $\mu\text{m}$  and the diffraction plates were developed in a Ditabis Micron scanner. To correctly interpret any preferred orientation or texture-related effects in the TEM images of the samples, the objective stigmatism of the electron beam was corrected by ensuring the fast Fourier transform was circular over amorphous carbon film before collecting data from the sample. Selected images were initially analysed using ImageJ<sup>24</sup> and any further processing was performed by means of bespoke scripts written in Python using NumPy, matplotlib and HyperSpy libraries<sup>25-27</sup>.

## Results and Discussion

### *Synthetic gypsum and bassanite*

We employed a combination of high-resolution (HR), bright field (BF) and dark field (DF) TEM imaging and electron diffraction to explore from the meso- to the nanoscale the internal structure and crystallographic properties of synthetic gypsum and bassanite single crystals. Fig. 1A shows a low-magnification energy-filtered BF image of a gypsum crystal synthesized from a 50 mM  $\text{CaSO}_4$

solution and aged for 2 days at room temperature. The resulting crystal is anisotropic in shape with the elongated direction parallel to the *c*-axis and exhibits straight facets. The out-of-plane thickness of the crystal centre in the highest contrast regions is > 400 nm as calculated by the log-ratio (relative) method<sup>28</sup> from the low loss electron energy loss spectra. This means that the bulk of the crystal in the field of view in Fig. 1A is not suitable for high resolution electron imaging, because it is too thick to obtain a sufficiently high signal-to-noise ratio from the CCD without significantly increasing the exposure time (which would cause beam damage to the material). However, the planes of the crystal facets do not intersect with each other at 90° (010, 120, -111 and 011 faces, see a schematic inset in Fig. 1A), and therefore the external crystal perimeter is characterized by a much thinner region. The thickness contrast in the TEM image of a thin-edge region (parallel to the crystal long-axis) of the single crystal (Fig. 1B) gradually increases from right to left, which is caused by the aforementioned increase in thickness towards the central part of the crystal. The observed structure does not represent a typically expected homogeneous and continuous internal single crystal appearance (e.g., compare with single crystals of fosterite and olivine shown in the Electronic Supplementary Information: Fig. S1). One can see that within the field of view the structure appears to be polycrystalline-like, where individual grains are distinguishable and exhibit a preferred orientation parallel to *c*-axis of the crystal. This is confirmed by the fast Fourier transform from the image (FFT, Fig. 1C), which contains an elliptically-shaped diffused low-angle scattering pattern localized around the centre of the FFT. Only faint lattice fringes can be seen, which suggests that the individual grains are poorly crystalline, and/or that the orientation of some of the grains is mismatched. The fast Fourier transform of the image (Fig. 1C) shows also one set of weak diffraction maxima corresponding to the same *d*-spacing. This indicates that the grains exhibiting lattice fringes are

crystallographically co-aligned. Overall this TEM analysis suggests that a gypsum single crystal is built of smaller nanoparticles that are slightly misaligned with each other.

The selected area electron diffraction (SAED) pattern of the crystal shown in Fig. 1A, confirms that the analysed crystal is a single gypsum crystal (Fig. 1D). The diffraction pattern contains only discrete diffraction peaks from a single crystallographic orientation. However, the recorded diffraction maxima exhibit very strong angle-dependent broadening effects exceeding  $>1^\circ$  at FWHMs. In single crystals, such effects, even when far smaller in magnitude, are typically attributed to a strong mosaicity *e.g.* <sup>29–31</sup>. The mosaicity is a measure of the misalignment of crystallographic sub-domains building up a single crystal. In general terms the division into sub-domains is a consequence of defects in the crystal lattice and does not necessarily mean that these domains physically constitute individual grain-like units. Nevertheless, the mosaicity in mesocrystals could be directly associated with the actual constituent nanosized sub-units. One can in fact identify the individual crystallographic domains in a mesocrystal, and hence evaluate their size, by performing DFTEM imaging with the diffracted beam corresponding to one of the diffraction maxima. Using this approach we show that a DFTEM image of the single gypsum crystal from Fig. 1A represents its bright field counterpart (Fig. 1E). The high intensity (white) in the DFTEM image originates from the regions of interest, which are oriented in such a way that they fulfil the Bragg condition corresponding to a selected diffracted beam. Hence, for a homogeneous single crystal these regions should exhibit a high uniform intensity (see ESI: Fig. S1 from fosterite). Furthermore, for a crystal of gradually changing thickness, as in Fig. 1A, the intensity should gradually decrease with increasing crystal thickness. In order to be able to consider these two effects more clearly we enhanced the contrast in Fig. 1E using histogram equalization. This was performed locally with respect to the limited-size regions of the highest contrast (rather than the entire image). Additionally, the gray-scale intensity was remapped 1:1 to



a fake-color perceptually uniform ‘inferno’ scale<sup>26</sup> resulting in the enhanced image presented in Fig. 1F, where bright yellow/orange regions correspond to areas of high diffraction contrasts (bright yellow > orange). The intensity decreases gradually perpendicular to the perimeter of the crystal and its in-plane long axis, which is equivalent to the direction in which the thickness of the crystal increases (inset I, Fig. 1F) as evidenced in the BFTEM image (Fig. 1A). On the other hand, abrupt contrast variations parallel to the long central axis of the crystal, originate from the misalignment between the scattering domains (*i.e.*, mosaicity). Each individual bright spot represents a single scattering domain, which are discontinuously distributed and appear to be anisotropic in shape with their long axis orientated parallel to the long axis of the crystal. This is confirmed by the average of a 2D fast Fourier transform series (FFT, inset II in Fig. 1F) calculated along the edges of the crystals (regions with the highest intensity). The compound FFT has an elliptical shape rotated in such a way that its short axis is parallel to the long axis of the crystal, and thus corresponds to the long dimension of the anisotropic scattering domains in Fig. 1F. Thus, the FFT shown in inset II points to a preferred orientation of the scattering domains. The dimension of the scattering domains is ~10-20 nm (direction perpendicular to the long axis of the crystal). In fact the presence of such orientated anisotropic domains is also additionally represented in the diffraction pattern in Fig. 1D. The SAED contains characteristic streaks in [001] direction (marked with dashed green arrows). This again indicates the presences of very thin platelet-like or lamellae-like domains orientated in the direction parallel to the long axis of the crystal. On the whole, the results from DFTEM corroborate those from TEM shown in Fig. 1B. The DF imaging is typically performed at low-magnification (*i.e.* low dose) which is highly beneficial because TEM (Fig. 1B) inherently increases the risk of beam damage to a highly hydrated sample such as gypsum<sup>32</sup>. We did not observe any obvious changes in the area imaged during our TEM

measurements, but DFTEM further ensured that our observations did not contain any significant artifacts.

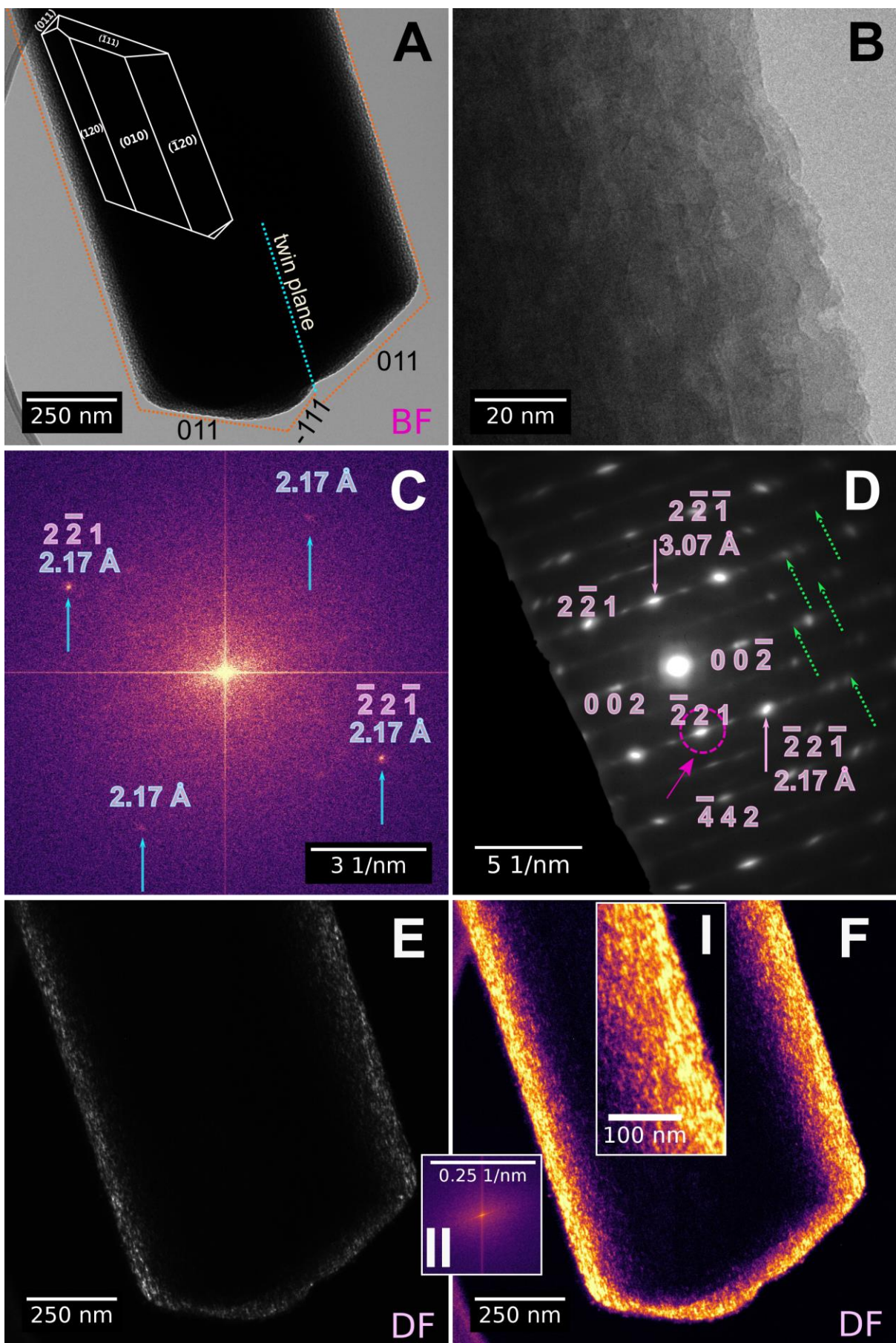


Fig. 1. TEM analysis of a representative gypsum crystal precipitated from a 50 mM  $\text{CaSO}_4$  solution and equilibrated for 2 days with this solution at room temperature. A) Bright field (BF) TEM image; schematics of the planes of crystal facets characteristic for gypsum; flux:  $\sim 650 \text{ e}^- \text{Å}^{-2} \text{s}^{-1}$ , estimated received fluence  $\sim 1 \times 10^{25} \text{ e}^- / \text{m}^2$ ; B) BFTEM image from a thin region located on the right edge of the crystal; flux:  $\sim 94 \text{ k e}^- \text{Å}^{-2} \text{s}^{-1}$ , estimated received fluence  $\sim 1 \times 10^{26} \text{ e}^- / \text{m}^2$ ; C) fast Fourier transform (FFT) of image (B). The indexed reflections and  $d$ -spacings are characteristic for gypsum<sup>33</sup>; D) SAED pattern collected from the centre of the gypsum crystal shown in (A) with selected reflections and  $d$ -spacings labelled; the dashed circle marks the diffracted beam used for DF imaging; the dashed green arrows point to a characteristic streaking present in the diffraction pattern in [001] direction; E) unprocessed DF image corresponding to (A); F) DF image from (E) with enhanced contrast using a local histogram equalization technique and with the intensity remapped to an ‘inferno’ scale<sup>26</sup>; inset I – zoom-in of the selected region of the main image; inset II – an average FFT calculated for the series taken along the left edge of the crystal.

To assess how the internal (mesoscale)-structure of single gypsum crystals compare to other calcium sulfate phases synthesized from solution we also analysed bassanite crystals ( $\text{CaSO}_4 \cdot 0.5\text{H}_2\text{O}$ ). Phase-pure bassanite can be directly made from solution by conducting the synthesis at low water activity<sup>1,21,33–35</sup>. We prepared bassanite samples following this strategy, where hemihydrate formed from a 50 mM  $\text{CaSO}_4$  solution with very high salinity (4.3 M NaCl) at  $T_{\text{min}} = 80 \text{ °C}$  (see Experimental and ref<sup>21</sup>). In Fig. 2A we present a BF image of a representative bassanite crystal that, similar to the gypsum crystal shown in Fig. 1, shows straight facets and a regular form. The analyses by SAED (Fig. 2B) confirmed this to be a single bassanite crystal and the individual diffraction spots again exhibited angle-dependent broadening. This diffraction pattern also exhibited streaking (dashed green arrows) in [001] direction, which could be explained in terms of thin anisotropic subunits oriented parallel to the long axis of the crystal. The observed bassanite crystal was significantly thinner than the gypsum crystal shown in Fig 1. The calculated thickness was only  $\sim 150 \text{ nm}$ , and therefore the DFTEM image revealed a

significantly higher level of detail from the interior of the crystal in addition to its perimeters (Fig. 2C). The corresponding contrast-enhanced image (Fig. 2D) shows that the bassanite single crystal is also composed of anisotropic nano-sized scattering domains aligned parallel to the long axis of the crystal (see FFT in inset I, Fig. 2D). These domains form locally parallel lines (inset II, Fig. 2D). Overall, the size and spatial arrangement of these domains are practically indistinguishable from those documented for the single gypsum crystal (Fig. 1).



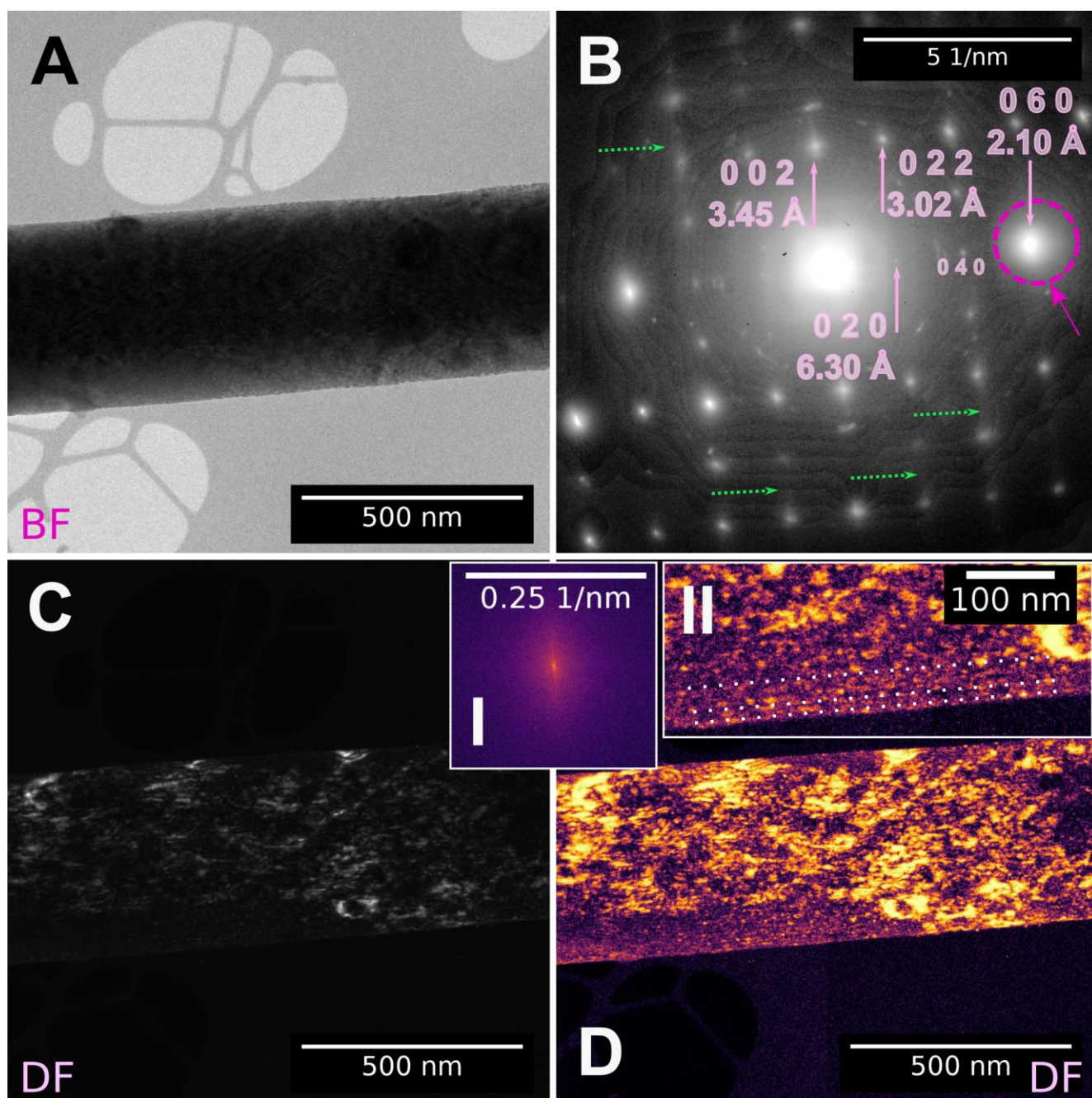


Fig. 2. TEM analysis of a representative bassanite crystal from  $\text{CaSO}_4$  50 mM and aged for 2 days in 4.3 M NaCl solution at 80 °C. A) BFTEM image; flux:  $\sim 650 \text{ e}^- \text{Å}^{-2} \text{s}^{-1}$ , estimated received fluence  $\sim 1 \times 10^{25} \text{ e}^-/\text{m}^2$ ; B) SAED taken from the center of a bassanite crystal from (A); the indices and  $d$ -spacings of the selected diffraction spots are provided; the dashed circle marks the diffracted beam used for dark field imaging; the dashed green arrows point to a characteristic streaking present in the diffraction pattern in [001] direction; C) unprocessed DFTEM image corresponding to (A); D) DF image with enhanced contrast and with an intensity remapped to an 'inferno' scale<sup>26</sup>; inset I – an average FFT calculated for the series taken along the entire long axis of the crystal; inset II – blow-up of

the selected region of the main image. Individual scattering domains form parallel lines some of which are highlighted by dotted lines for ease of viewing.

### *Natural calcium sulfate phases*

Under natural conditions calcium sulfate phases, in particular gypsum and anhydrite, are known to grow into single crystals that can easily reach many centimetres or even meters in size<sup>22,36–38</sup>. The question arises if such big natural crystals also grow and develop structures resembling those presented above for the synthetic phases. For this purpose we performed analysis on natural single crystals of gypsum (a piece of ~3 cm in length chipped from a larger crystal), and anhydrite (~1 cm in length). To analyse such large crystals we prepared ~15  $\mu\text{m}$  x 4  $\mu\text{m}$  sections that were thinned to foils of ~100 nm in thickness using a focused ion beam (FIB, see Experimental). The foils were cut from the regions located in the bulk of the crystal. In the case of gypsum crystals this processing step introduced apparent damages to the crystals (primarily due to an ongoing dehydration in vacuum) and the foils were not stable during the TEM analysis. Interestingly this was not the case for the anhydrous calcium sulfate, anhydrite; we analysed this sample further as it was very stable in the vacuum and not significantly affected by the electron or ion beams for the operating conditions used for this work. Fig. 3A shows a BF image of such an anhydrite thin-foil. In this case, the observed contrast variations at the length-scale of 10-20 nm form a regular pattern, which we attribute to the defect structure of the material. The SAED in the inset confirms that we are dealing with a single crystal, similar to the synthetic calcium sulfate crystals (Figs. 1 & 2), the diffraction pattern points to a significant mosaicity as evidenced by the elliptical shape of the diffraction spots. DF imaging (Fig. 3B) highlights ~10-20 nm sized discontinuous diffraction domains within the crystal, which coincide with the microstructural pattern observed in BF (Fig. 3A). This is in stark contrast with the thin-

foils from the single crystals of our fosterite crystal (Fig. S1), in which the crystallographic domains are continuous throughout the micron length-scales of the region of interest. Similar to the synthetic gypsum and bassanite, the nano-domains in the natural anhydrite are aligned in a single direction as confirmed by the anisotropic shape of the FFT obtained from the DFTEM image (inset Fig 3B). The high stability of the anhydrite thin-foil allowed us to perform high-resolution imaging (Fig. 3C), which confirmed the overall single-crystalline nature of the anhydrite sample (see FFT in the inset in Fig. 3C). However, the HRTEM image also contains clear areas of different contrast (darker) that are less ordered than the surrounding crystalline areas (lighter). We highlighted those by performing FFT filtering of the image in Fig. 3C and then performing the inverse FFT reconstruction and applying a fake colour map. The resulting Fig. 3D clearly highlights the nanocrystalline domains (10-20 nm in size) separated from each other by disordered areas of several nanometres in width.



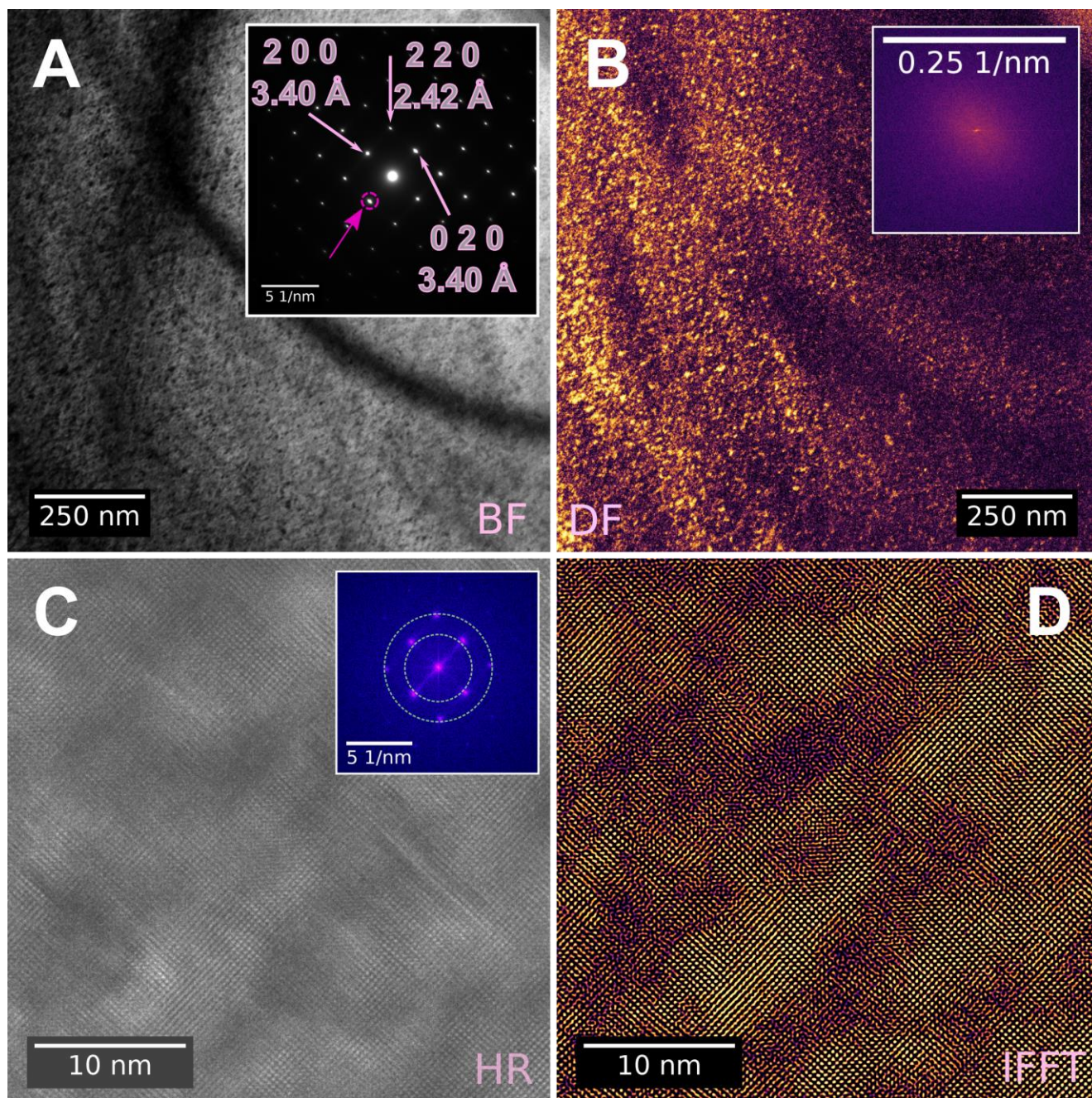


Fig. 3. TEM analysis of a FIB thin-foil cut from a natural anhydrite single crystal (see Fig. S2). A) BFTEM image; flux:  $\sim 650 \text{ e} \cdot \text{\AA}^{-2} \text{s}^{-1}$ , estimated received fluence:  $2 \times 10^{25} \text{ e}^{-}/\text{m}^2$ ; the inset shows an SAED pattern taken from the field of view; the dashed circle marks the diffracted beam used for DF imaging; the indices and  $d$ -spacings of the selected diffraction spots are provided; B) DFTEM image corresponding to (A) with enhanced contrast and with the intensity remapped to an 'inferno' scale<sup>26</sup>; the inset shows an FFT calculated for the image in (B); C) the HRTEM image of the foil; flux:  $\sim 800 \text{ k e} \cdot \text{\AA}^{-2} \text{s}^{-1}$ , estimated received fluence  $\sim 1 \times 10^{27} \text{ e}^{-}/\text{m}^2$ ; the inset shows the FFT of the HRTEM image and indicates that the lattice fringes in (C) originate from a single orientation of a crystal; the green dashed circles mark

the inner and the outer diameters of the filter ring used to obtain (D); D) the IFFT-filtered image from C) (inverse FFT), with an 'inferno' colour map applied.

## Implications and Outlook

Our microscopic analysis of both lab-grown and natural single crystals of the various calcium sulfate phases shows that they all share remarkably similar nano/meso-structures. The considered single crystals of gypsum, bassanite and anhydrite are composed of slightly misaligned anisotropic crystallographic domains, which are ~10-20 nm in size. Hence, we classify the observed crystals as mesocrystals, yet following the current consensus we point out that this classification is based on their final structure, which essentially does not provide on its own a sufficient evidence for the non-classical, particle-mediated, growth mechanism<sup>39,40</sup>. However, in our previous work based, on scattering experiments and theory<sup>1-3,41</sup>, we found that the crystallization of calcium sulfate phases occurs through the coalescence and growth of primary particles within surface fractal aggregates ("brick-in-a-wall")<sup>3</sup>. We postulated that this initial step involved a framework structure as a plausible common precursor to gypsum, bassanite and anhydrite<sup>1,2</sup>. Our scattering data show that the primary particles in this framework structure are nanosized Ca-SO<sub>4</sub>, internally anhydrous, clusters (<3 nm in length), which during the actual crystallization process increase in dimension and polydispersity to form larger structural nanoparticulate sub-units within the growing, final, crystals. However, the fact that after the onset of crystallization structural sub-units are still distinguishable strongly indicates that misalignment and voids exist between the sub-units, similar to what can be seen in Fig. 3D. Fig. 4 shows a SAXS pattern, adapted from our previous work<sup>2</sup>, of gypsum crystals synthesized from solution 4 hours after the onset of precipitation, which is already beyond the final stage of the

nucleation process<sup>29</sup>. At this point the 2D SAXS patterns were anisotropic (Fig. 4A), i.e. stronger scattering at higher angles was observed in the direction almost parallel to the  $y$  axis of the 2D detector plane (vertical direction), and thus normal to the  $x$  axis (horizontal direction). This anisotropy is further highlighted by the reduction to direction-dependent 1D scattering patterns (Fig. 4B). Taking into account that gypsum forms elongated crystals, i.e. needles<sup>33</sup>, whose long axis became aligned with the solution flow through a horizontally mounted capillary used for the *in situ* SAXS measurements<sup>2,29</sup> such an anisotropic scattering pattern is expected, if within the accessible  $q$ -range there are orientation-dependent internal variations in the microstructure of the large crystalline particles with respect to their long-axes. Thus, gypsum crystals are composed of smaller structural features (e.g. nanoparticles), which are oriented with respect to each other. The larger dimension of these anisotropic nano-domains are oriented parallel to the flow and the long-axis of the crystals containing these particles, and *vice versa* (inset in Fig. 4B). The intensity of both direction-dependent 1D scattering patterns, i.e. parallel and perpendicular to the flow direction, scale with  $\sim q^{-4}$  for  $q_0 < \sim 0.5 \text{ nm}^{-1}$  (Fig. 4B), originating from the internal and external interfaces of gypsum crystals. For  $q_0 > \sim 0.5 \text{ nm}^{-1}$  the scattering intensity of both patterns scales with  $q^{-4}$ , originating from structural features with a characteristic size of  $< 2\pi/q_0 = \sim 13 \text{ nm}$  (equivalent to the radius of gyration). Therefore, we define these crystals as “brick-in-a-wall” surface fractal aggregates<sup>3</sup>. At long length-scales (low- $q$ ) these objects appear to be homogeneous (single crystals) with their scattering patterns dominated by the interface between the them and the surrounding solution (i.e.  $I(q) \propto q^{-3}$   <sup>$a \geq -4$</sup> ). In contrast, at short length-scales (high- $q$ ), the scattering patterns represent form factors of the building units of these crystals. These are very densely packed with respect to each other (in contrast to classical mass fractals), yet still clearly distinguishable.



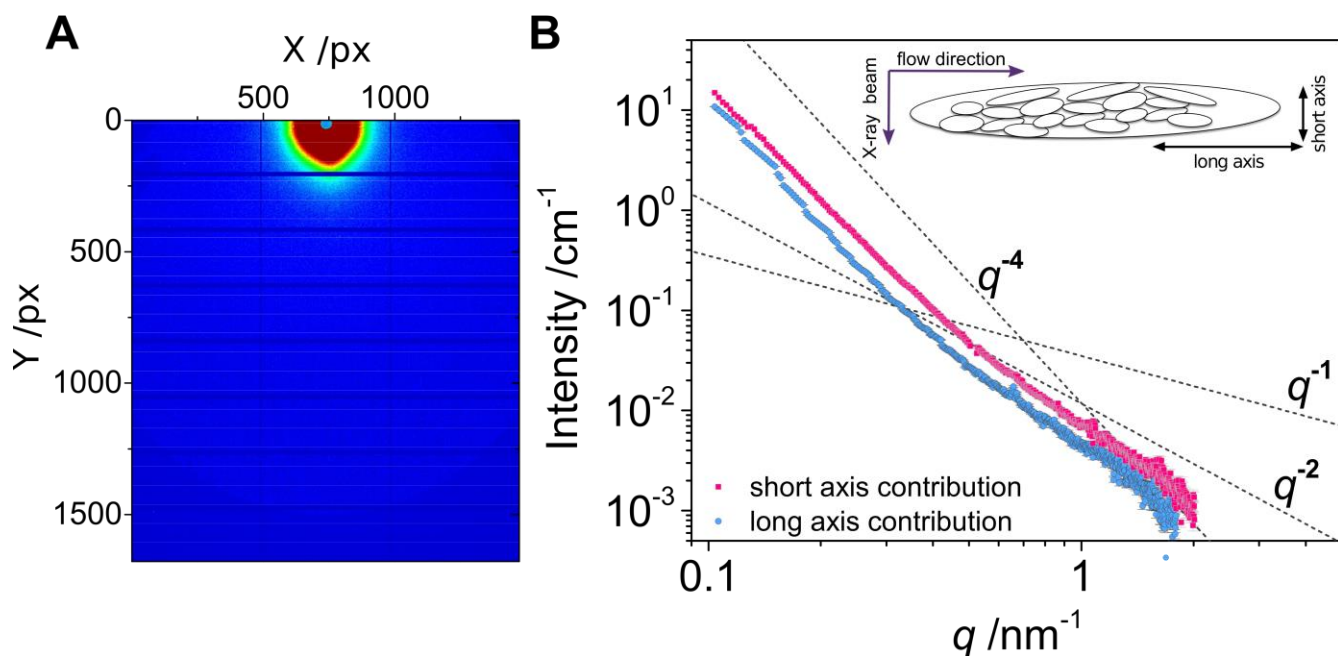


Fig. 4., SAXS pattern acquired from a solution containing gypsum crystals synthesized and aged for 4 hours in a solution. A) 2D SAXS patterns from a 50 mM  $\text{CaSO}_4$  solution equilibrated at 12 °C for 4 hours after the onset of precipitation. Intensity scale color-coding: red – high, blue – low; B) 1D angle-dependent SAXS curves from (A) obtained by averaging pixels at similar  $q$  and limited to ca.  $\pm 3^\circ$  angle off the direction indicated by the chosen azimuthal angle (the equatorial and meridional directions of the elliptical 2D pattern). The change in the  $I(q)$  dependence of the scattering exponent in different parts of the 1D patterns are also shown to emphasize the differences in the high- $q$  part of the data (dashed lines). Inset: schematic representation of the morphology of flow-oriented particles. (adapted from ref. <sup>2</sup>, where further experimental details can be found).

Our data show that the re-structuring and coalescence processes by no means continue until a near-perfectly homogeneous single crystal is obtained, and instead it comes to a stop or at least significantly slows down. This growth behaviour can be rationalized if we consider that during the early stages of precipitation all calcium sulfate crystals appear to grow through the reorganization and coalescence of aggregates rather than through unit addition. In order to obtain well-ordered anhydrous cores of  $\text{Ca-SO}_4$  surrounded by  $\text{H}_2\text{O}$  layers (as found in gypsum),  $\text{H}_2\text{O}$  channels (bassanite), or fully dehydrated crystals (anhydrite), the nanoparticle aggregates

must radically transform from a local less-ordered structure to a more ordered crystal. Hence, any mass transport processes inside such aggregates must be subject to slow diffusion processes compared to transport in a bulk aqueous solution. This process thus yields a final imperfect mesocrystal, composed of smaller domains rather than a perfectly continuous single crystal. This early-stage crystallization however, does not exclude growth by ion-by-ion addition<sup>37</sup>, a process that will still dominate e.g., at low supersaturations and essentially should yield far more perfect single crystals. Furthermore, the nano-scale misalignment of the structural sub-units within crystals might propagate through the length-scales, is expressed macroscopically as spherulites (formed at low supersaturations) and multiple twins (Fig. 5a), or as misaligned zones/domains in large single crystals, as one can clearly see in the giant crystals from Naica grown at extreme low levels of supersaturation<sup>36</sup> (Fig. 5B).

In conclusion, the data presented in this work provide compelling evidence that the particle-mediated nucleation pathway is “fossilized”, i.e. retaining the initial nanoparticle aggregate structure, inside of the structure of all three calcium sulphate phases. This finding is paramount to explain the patterns observed in natural calcium sulfate formations, but is also essential to improve our control over the crystallization of calcium sulfate, an industrially relevant material (e.g., *plaster of Paris*, scalant).

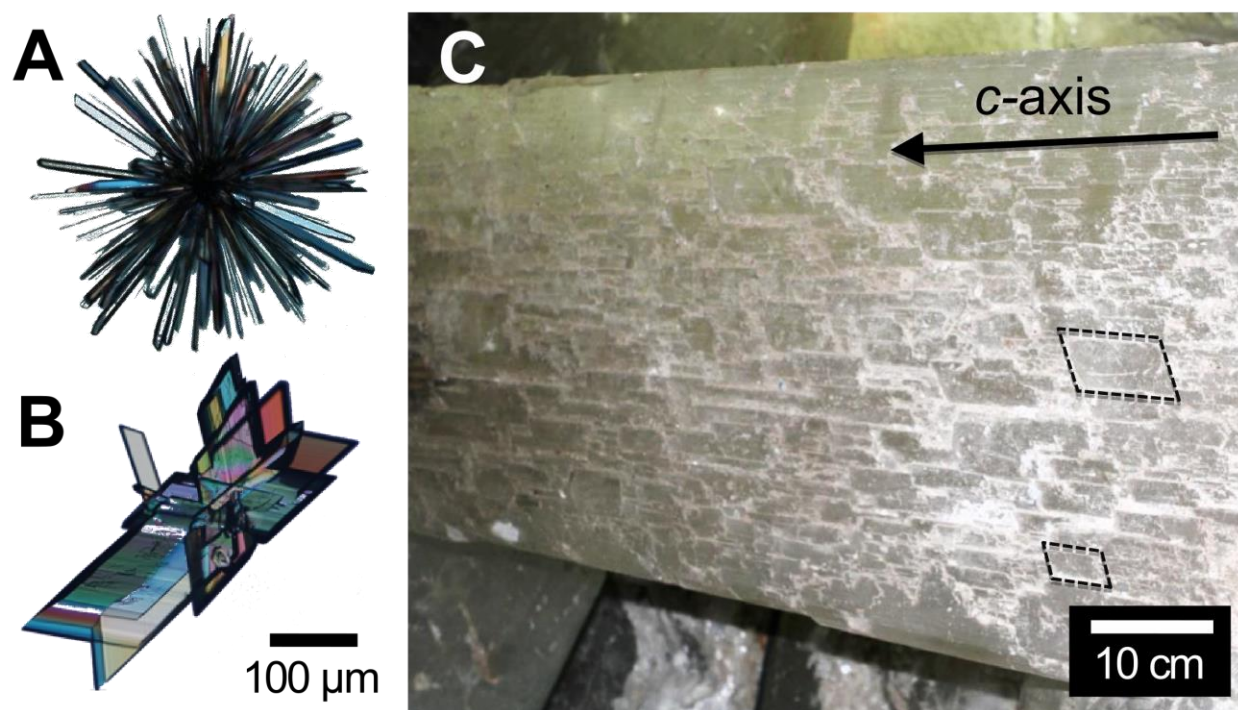


Fig. 5. Typical (A) spherulite and (B) multiple twin morphologies observed for lab grown gypsum crystals at the same magnification ; (C) A giant gypsum single crystal from Naica, Chihuahua, Mexico. Smaller co-aligned domains (a few are delineated with dotted black parallels) are clearly visible in the bulk of the crystal. Arrows indicate the *c*-axes of the crystal.

## Acknowledgments

This research was made possible by a Marie Curie grant from the European Commission: the NanoSiAl Individual Fellowship, Project No. 703015 to TMS. We also acknowledge the financial support of the Helmholtz Recruiting Initiative grant No. I-044-16-01 to LGB.

## References

- (1) Van Driessche, A. E. S.; Stawski, T. M.; Benning, L. G.; Kellermeier, M. Calcium Sulfate Precipitation Throughout Its Phase Diagram. In *New Perspectives on Mineral Nucleation and Growth*; Springer International Publishing: Cham, 2017; pp 227–256.
- (2) Stawski, T. M.; van Driessche, A. E. S.; Ossorio, M.; Diego Rodriguez-Blanco, J.; Besselink, R.; Benning, L. G. Formation of Calcium Sulfate through the Aggregation of Sub-3 Nanometre Primary Species. *Nat. Commun.* **2016**, 7, 11177.
- (3) Besselink, R.; Stawski, T. M.; Van Driessche, A. E. S. S.; Benning, L. G. Not Just Fractal Surfaces, but Surface Fractal Aggregates: Derivation of the Expression for the Structure Factor and Its Applications. *J. Chem. Phys.* **2016**, 145 (21), 211908.
- (4) Darwin, C. G. The Reflexion of X-Rays from Imperfect Crystals. *London, Edinburgh, Dublin Philos. Mag. J. Sci.* **1922**, 43 (257), 800–829.
- (5) Cölfen, H.; Yu, S.-H. Biomimetic Mineralization/Synthesis of Mesoscale Order in Hybrid Inorganic–Organic Materials via Nanoparticle Self-Assembly. *MRS Bull.* **2005**, 30 (10), 727–735.
- (6) Niederberger, M.; Cölfen, H. Oriented Attachment and Mesocrystals: Non-Classical Crystallization Mechanisms Based on Nanoparticle Assembly. *Phys. Chem. Chem. Phys.* **2006**, 8 (28), 3271–3287.
- (7) De Yoreo, J. J.; Gilbert, P. U. P. A.; Sommerdijk, N. A. J. M.; Penn, R. L.; Whitlam, S.; Joester, D.; Zhang, H.; Rimer, J. D.; Navrotsky, A.; Banfield, J. F.; et al. Crystallization by Particle Attachment in Synthetic, Biogenic, and Geologic Environments. *Science (80-. ).* **2015**, 349 (6247), aaa6760.

- (8) Zhou, L.; O'Brien, P. Mesocrystals: A New Class of Solid Materials. *Small* **2008**, *4* (10), 1566–1574.
- (9) Sturm (née Rosseeva), E. V.; Cölfen, H. Mesocrystals: Structural and Morphogenetic Aspects. *Chem. Soc. Rev.* **2016**, *45* (21), 5821–5833.
- (10) Cölfen, H. (Helmut); Antonietti, M. *Mesocrystals and Nonclassical Crystallization*; Wiley, 2008.
- (11) Rao, A.; Cölfen, H. Mineralization Schemes in the Living World: Mesocrystals. In *New Perspectives on Mineral Nucleation and Growth*; Springer International Publishing: Cham, 2017; pp 155–183.
- (12) Agthe, M.; Wetterskog, E.; Mouzon, J.; Salazar-Alvarez, G.; Bergström, L. Dynamic Growth Modes of Ordered Arrays and Mesocrystals during Drop-Casting of Iron Oxide Nanocubes. *CrystEngComm* **2014**, *16* (8), 1443–1450.
- (13) Yang, P.; Kim, F. Langmuir - Blodgett Assembly of One-Dimensional Nanostructures. *ChemPhysChem*. Wiley-Blackwell June 17, 2002, pp 503–506.
- (14) Li, L.; Yang, Y.; Ding, J.; Xue, J. Synthesis of Magnetite Nanooctahedra and Their Magnetic Field-Induced Two-/Three-Dimensional Superstructure. *Chem. Mater.* **2010**, *22* (10), 3183–3191.
- (15) Bergström, L.; Sturm née Rosseeva, E. V.; Salazar-Alvarez, G.; Cölfen, H. Mesocrystals in Biominerals and Colloidal Arrays. *Acc. Chem. Res.* **2015**, *48* (5), 1391–1402.
- (16) Ma, M. G.; Cölfen, H. Mesocrystals - Applications and Potential. *Current Opinion in Colloid and Interface Science*. Elsevier April 1, 2014, pp 56–65.



- (17) Penn, R. L.; Li, D.; Soltis, J. A. A Perspective on the Particle-Based Crystal Growth of Ferric Oxides, Oxyhydroxides, and Hydrous Oxides. In *New Perspectives on Mineral Nucleation and Growth*; Springer International Publishing: Cham, 2017; pp 257–273.
- (18) Penn, R. L. Imperfect Oriented Attachment: Dislocation Generation in Defect-Free Nanocrystals. *Science (80-. )*. **1998**, *281* (5379), 969–971.
- (19) Yuwono, V. M.; Burrows, N. D.; Soltis, J. A.; Penn, R. L. Oriented Aggregation: Formation and Transformation of Mesocrystal Intermediates Revealed. *J. Am. Chem. Soc.* **2010**, *132* (7), 2163–2165.
- (20) Wu, H.; Yang, Y.; Ou, Y.; Lu, B.; Li, J.; Yuan, W.; Wang, Y.; Zhang, Z. Early Stage Growth of Rutile Titania Mesocrystals. *Cryst. Growth Des.* **2018**, *18* (8), 4209–4214.
- (21) Ossorio, M.; Van Driessche, A. E. S.; Pérez, P.; García-Ruiz, J. M. The Gypsum–anhydrite Paradox Revisited. *Chem. Geol.* **2014**, *386*, 16–21.
- (22) Van Driessche, A. E. S.; Canals, A.; Ossorio, M.; Reyes, R. C.; García-Ruiz, J. M. Unraveling the Sulfate Sources of (Giant) Gypsum Crystals Using Gypsum Isotope Fractionation Factors. *J. Geol.* **2016**, *124* (2), 235–245.
- (23) Wirth, R. Focused Ion Beam (FIB) Combined with SEM and TEM: Advanced Analytical Tools for Studies of Chemical Composition, Microstructure and Crystal Structure in Geomaterials on a Nanometre Scale. *Chem. Geol.* **2009**, *261* (3–4), 217–229.
- (24) Rueden, C. T.; Schindelin, J.; Hiner, M. C.; DeZonia, B. E.; Walter, A. E.; Arena, E. T.; Eliceiri, K. W. ImageJ2: ImageJ for the next Generation of Scientific Image Data. *BMC Bioinformatics* **2017**, *18* (1), 529.

- (25) Oliphant, T. E. *A Guide to NumPy*; 2006; Vol. 1.
- (26) Hunter, J. D. Matplotlib: A 2D Graphics Environment. *Comput. Sci. Eng.* **2007**, 9 (3), 99–104.
- (27) de la Pena, F.; Fauske, V. T.; Burdet, P.; Prestat, E.; Jokubauskas, P.; Nord, M.; Ostasevicius, T.; MacArthur, K. E.; Sarahan, M.; Johnstone, D. N.; et al. HyperSpy v1.4.1. **2018**.
- (28) Malis, T.; Cheng, S. C.; Egerton, R. F. EELS Log-Ratio Technique for Specimen-Thickness Measurement in the TEM. *J. Electron Microsc. Tech.* **1988**, 8 (2), 193–200.
- (29) Bellamy, H. D.; Snell, E. H.; Lovelace, J.; Pokross, M.; Borgstahl, G. E. O. The High-Mosaicity Illusion: Revealing the True Physical Characteristics of Macromolecular Crystals. *Acta Crystallogr. Sect. D Biol. Crystallogr.* **2000**, 56 (8), 986–995.
- (30) Snell, E. H.; Weisgerber, S.; Helliwell, J. R.; Hölzer, K.; Schroer, K. Improvements in Lysozyme Protein Crystal Perfection through Microgravity Growth. *Acta Crystallogr. D. Biol. Crystallogr.* **1995**, 51 (Pt 6), 1099–1102.
- (31) Ferrari, C.; Zanotti, L.; Zappettini, A.; Arumainathan, S. Mosaic GaAs Crystals for Hard X-Ray Astronomy; Goto, S., Khounsary, A. M., Morawe, C., Eds.; International Society for Optics and Photonics, 2008; Vol. 7077, p 707700.
- (32) Lee, M. R. The Petrography, Mineralogy and Origins of Calcium Sulphate within the Cold Bokkeveld CM Carbonaceous Chondrite. *Meteoritics* **1993**, 28 (1), 53–62.
- (33) Van Driessche, A. E. S.; Benning, L. G.; Rodriguez-Blanco, J. D.; Ossorio, M.; Bots, P.; García-Ruiz, J. M. The Role and Implications of Bassanite as a Stable Precursor Phase to Gypsum Precipitation. *Science (80-. ).* **2012**, 336 (6077), 69–72.
- (34) Tritschler, U.; Van Driessche, A. E. S.; Kempter, A.; Kellermeier, M.; Cölfen, H. Controlling the

Selective Formation of Calcium Sulfate Polymorphs at Room Temperature. *Angew. Chemie Int. Ed.* **2015**, *54* (13), 4083–4086.

- (35) Tritschler, U.; Kellermeier, M.; Debus, C.; Kempter, A.; Coelfen, H. A Simple Strategy for the Synthesis of Well-Defined Bassanite Nanorods. *CrystEngComm* **2015**.
- (36) Van Driessche, A. E. S.; Garcia-Ruiz, J. M.; Tsukamoto, K.; Patino-Lopez, L. D.; Satoh, H. Ultraslow Growth Rates of Giant Gypsum Crystals. *Proc. Natl. Acad. Sci.* **2011**, *108* (38), 15721–15726.
- (37) Garcia-Guinea, J.; Morales, S.; Delgado, a.; Recio, C.; Calaforra, J. M. M.; García-Guinea, J.; Morales, S.; Delgado, a.; Recio, C.; Calaforra, J. M. M. Formation of Gigantic Gypsum Crystals. *J. Geol. Soc. London.* **2002**, *159* (4), 347–350.
- (38) Foshag, W. F. The Selenite Caves of Naica, Mexico. *Am. Mineral.* **1927**, *12* (6), 252–256.
- (39) Smeets, P. J. M.; Cho, K. R.; Sommerdijk, N. A. J. M.; De Yoreo, J. J. A Mesocrystal-Like Morphology Formed by Classical Polymer-Mediated Crystal Growth. *Adv. Funct. Mater.* **2017**, *27* (40), 1701658.
- (40) Kim, Y.-Y.; Schenk, A. S.; Ihli, J.; Kulak, A. N.; Hetherington, N. B. J.; Tang, C. C.; Schmahl, W. W.; Griesshaber, E.; Hyett, G.; Meldrum, F. C. A Critical Analysis of Calcium Carbonate Mesocrystals. *Nat. Commun.* **2014**, *5* (1), 4341.
- (41) Ossorio, M.; Stawski, T.; Rodríguez-Blanco, J.; Sleutel, M.; García-Ruiz, J.; Benning, L.; Van Driessche, A.; Ossorio, M.; Stawski, T. M.; Rodríguez-Blanco, J. D.; et al. Physicochemical and Additive Controls on the Multistep Precipitation Pathway of Gypsum. *Minerals* **2017**, *7* (8), 140.

# ***Electronic Supporting Information***

*to*

## ***Particle-mediated nucleation pathways are imprinted in the internal structure of calcium sulfate single crystals***

Tomasz M. Stawski<sup>1</sup>, Helen M. Freeman<sup>1,2</sup>, Alexander E.S. Van Driessche<sup>3</sup>, Jörn Hövelmann<sup>1</sup>,

Rogier Besselink<sup>1,3</sup>, Richard Wirth<sup>1</sup>, and Liane G. Benning<sup>1,4,5</sup>

<sup>1</sup>German Research Centre for Geosciences, GFZ, Interface Geochemistry, Telegrafenberg, 14473, Potsdam, Germany;

<sup>2</sup>School of Chemical and Process Engineering, University of Leeds, Woodhouse Lane, LS2 9 JT, Leeds, UK;

<sup>3</sup>Université Grenoble Alpes, CNRS, ISTERre, 1381 Rue de la Piscine, 38610 Gières, Grenoble, France;

<sup>4</sup>Geochemistry Group, Department of Earth Sciences, Free University of Berlin, Malteserstr. 74-100 / Building A, 12249 , Berlin, Germany.

<sup>5</sup>School of Earth and Environment, University of Leeds, Woodhouse Lane, LS2 9 JT, Leeds, UK;

**Keywords:** calcium sulfate; gypsum; bassanite; anhydrite; mesocrystal; non-classical; crystallisation

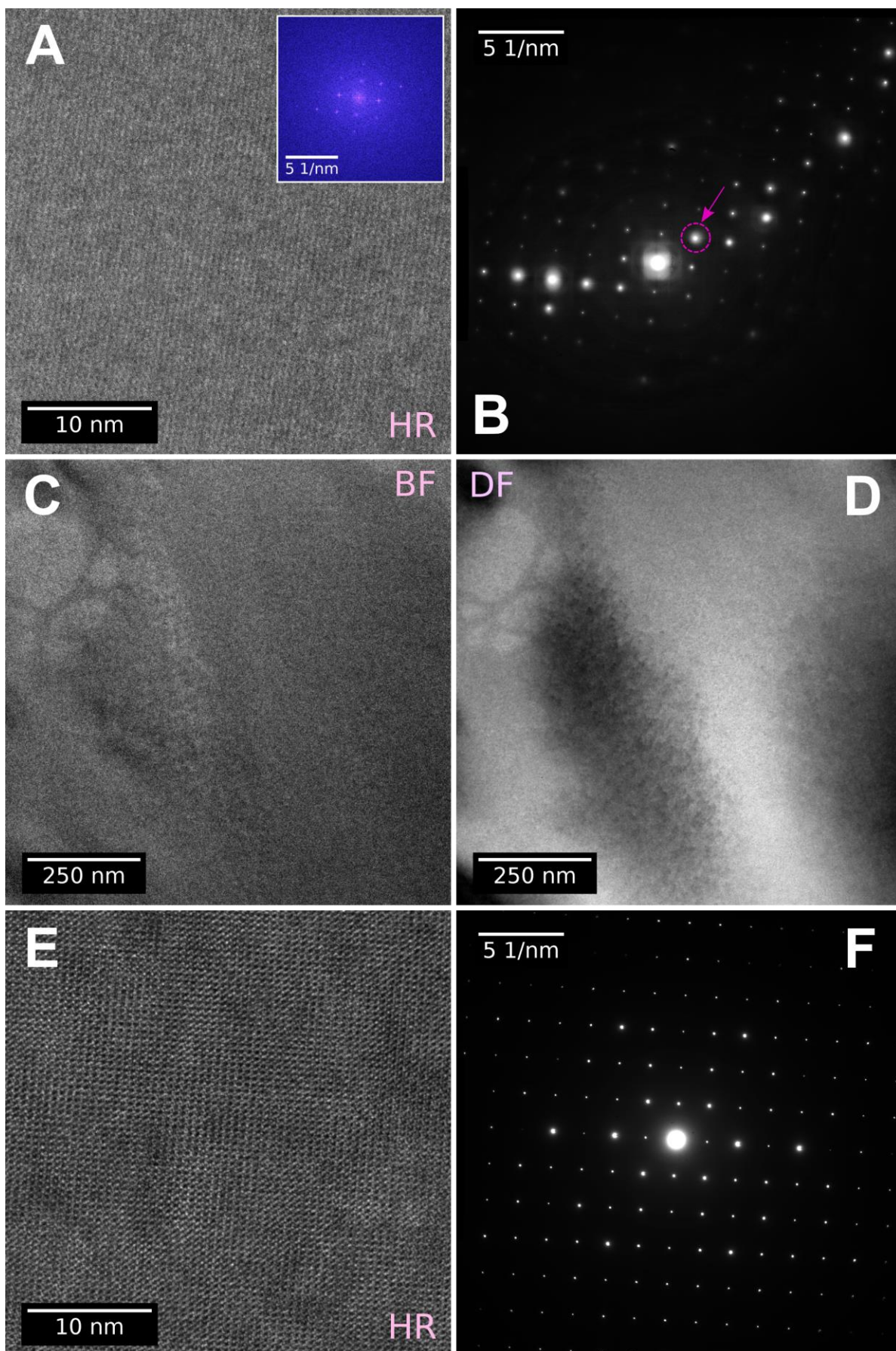


Figure S1. TEM analysis of a FIB thin-foil cut from a natural fosterite (nominally  $\text{Mg}_2\text{SiO}_4$ ) and generic olivine ( $(\text{Mg,Fe}^{2+})_2\text{SiO}_4$ ) single crystals. Electron beam current; A) HR image of fosterite showing clear and uniform lattice fringes in the entire field of view; flux:  $\sim 800\text{k } e\cdot\text{\AA}^{-2}\text{s}^{-1}$ , estimated received fluence  $\sim 1\text{e}27 \text{ } e^-/\text{m}^2$ ; the inset shows the FFT of the HR image and indicates that the lattice fringes originate from a single orientation of a crystal; B) SAED pattern of fosterite with the dashed circle marking the diffracted beam used for dark field imaging; C) low-magnification BF image of fosterite; flux:  $\sim 980 \text{ } e\cdot\text{\AA}^{-2}\text{s}^{-1}$ , estimated received fluence  $\sim 1\text{e}25 \text{ } e^-/\text{m}^2$  D) DFTEM image corresponding to (C) showing that the field of view is essentially crystallographically uniform, with the differences in contrast originating from the imperfections of the FIB foil, such as its warping; E) HR image of highly-crystalline olivine showing clear and uniform lattice fringes in the entire field of view; flux:  $\sim 800\text{k } e\cdot\text{\AA}^{-2}\text{s}^{-1}$ , estimated received fluence  $\sim 1\text{e}27 \text{ } e^-/\text{m}^2$ ; F) SAED pattern of olivine demonstrating a high-quality single crystalline nature of the sample.